Relativistic impulse approximation analysis of elastic proton scattering from He isotopes

Kaori Kaki*
Department of Physics, Shizuoka University, Shizuoka 422-8529, Japan
(Received 6 September 2013; published 30 January 2014)

Recent relativistic mean field (RMF) calculations have provided nuclear distributions of some isotopes whose mass numbers are much larger than atomic numbers. For helium isotopes, the RMF calculation seems to be inappropriate because of the small mass numbers; however, applicable results are obtained for ^{6,8}He nuclei. The author calculates observables of proton elastic scattering from the helium isotopes and discusses relations between observables and nuclear distributions of the isotopes by comparison of the calculated results with experimental data. The calculations are based on relativistic impulse approximation (RIA) at incident proton energy: 71 MeV for ^{4,6,8}He, 300 and 500 MeV for ^{4}He, and 0.7 GeV for ^{6}He. Scattering observables are predicted for ^{6,8}He at 200 MeV.

DOI: 10.1103/PhysRevC.89.014620 PACS number(s): 21.10.Gv, 24.10.Jv, 24.70.+s, 25.40.Cm

I. INTRODUCTION

Unstable nuclei are fruitful objects for nuclear physics because they provide new information about halo structure, magic numbers, nuclear matter properties, and many other things which are very different from stable nuclei. Helium isotopes, ^{6}He and ^{8}He, have extremely large values of neutron to proton ratios, and recent development of experimental technique has enabled us to take the proton elastic scattering data, especially analyzing power data at 71 MeV/nucleon [1–3].

Theoretical studies have been done on the optical potential and observables for proton elastic scattering from ^{6}He and ^{8}He. The differential cross section for ^{8}He target was calculated and compared with the data of Ref. [4] on the bases of the single-scattering approximation to the multiple-scattering expansion [5]. The angular distribution of the scattering observables was analyzed in terms of an eikonal approach in order to examine the matter distribution of the ^{8}He nucleolus [6]. For ^{6}He and ^{8}He nuclei the scattering observables were calculated in a full-folding optical model [7]. Dynamic polarization potentials were presented, which arise from neutron pickup coupled reaction channels, and were applied to proton elastic scattering from ^{6}He [8]. The $p + {}^{4,6,8}$He elastic scattering observables were analyzed with the optical potentials derived using the Glauber theory [9]. Brueckner-Hartree-Fock-based optical potential was calculated for helium isotopes as well as for lithium isotopes [10]. Predicted analyzing powers for ^{6}He and/or ^{8}He at 71 MeV in Refs. [5,7,8] are different from the experimental data [1–3], while Refs. [9,10] show good agreement with the data. The former has one adjustable parameter, the strength of the spin-orbit potential, and the latter reproduces the data with a specific choice of NN interactions and density distributions.

Calculations based on the relativistic impulse approximation (RIA) have succeeded in reproducing experimental data of proton elastic scattering from many nuclei at energies larger than 200 MeV, especially for observables with respect to spin. The purpose of this paper is to analyze the proton elastic scattering from helium isotopes on the basis of RIA. In order to calculate the optical potential the density distribution of the target nucleus is needed, which is provided by the relativistic mean field (RMF) calculation [11,12] since RMF calculation recently has provided nuclear distributions for many unstable and stable nuclei. However, helium isotopes seem to be too small for calculation with the RMF code, and only one adjustable parameter is introduced to make distributions realistic, of which detailed explanation is given in the following section.

In Sec. II, formulas on which the analysis is based are presented, and numerical results are given in Sec. III. Calculated results are compared to experimental data and predictions for proton elastic scattering at 200 MeV are also given in Sec. III. The summary of this study appears in Sec. IV.

II. FORMULATION

The Dirac equation containing the optical potential is described in momentum space as follows:

$$\{\gamma^0 E - \boldsymbol{\gamma}\cdot\boldsymbol{p}' - m\}\,\Psi(\boldsymbol{p}') - \int \frac{d^3p}{(2\pi)^3}\,\hat{U}(\boldsymbol{p}',\boldsymbol{p})\,\Psi(\boldsymbol{p}) = 0, \tag{1}$$

where $\Psi(\boldsymbol{p})$ is given by the Fourier transformation of the wave function in coordinate space:

$$\Psi(\boldsymbol{p}) = \int d^3r e^{-i\boldsymbol{p}\cdot\boldsymbol{r}}\Psi(\boldsymbol{r}), \tag{2}$$

where natural unit($\hbar = c = 1$) is taken.

In accordance with the prescription of the RIA [13,14], the Dirac optical potential is given in momentum space by

$$\begin{aligned}\hat{U}(\boldsymbol{p}',\boldsymbol{p}) &= -\frac{1}{4}\mathrm{Tr}_2\left\{\int \frac{d^3k}{(2\pi)^2}\hat{M}_{pp}\left(\boldsymbol{p},\boldsymbol{k}-\frac{\boldsymbol{q}}{2}\to\boldsymbol{p}',\boldsymbol{k}+\frac{\boldsymbol{q}}{2}\right)\hat{\rho}_p(\boldsymbol{k},\boldsymbol{q})\right\}\\ &\quad -\frac{1}{4}\mathrm{Tr}_2\left\{\int \frac{d^3k}{(2\pi)^2}\hat{M}_{pn}\left(\boldsymbol{p},\boldsymbol{k}-\frac{\boldsymbol{q}}{2}\to\boldsymbol{p}',\boldsymbol{k}+\frac{\boldsymbol{q}}{2}\right)\hat{\rho}_n(\boldsymbol{k},\boldsymbol{q})\right\},\end{aligned} \tag{3}$$

*spkkaki@ipc.shizuoka.ac.jp

where $\hat{\rho}_p$ and $\hat{\rho}_n$ are density matrices for protons and neutrons, respectively. The trace is over the γ matrices with respect to the target nucleons and the subscript 2 in the trace corresponds to the target nucleons.

As discussed in Ref. [14] it is known that the nuclear density generally varies more rapidly with $\boldsymbol{k}$ than the NN amplitude and is largest at $\boldsymbol{k} = 0$. Therefore, taking the optimal factorization into account, the optical potentials are written in the well-known $t\rho$ forms:

$$\hat{U}(\boldsymbol{p}', \boldsymbol{p}) = -\frac{1}{4}\mathrm{Tr}_2\left\{\hat{M}_{pp}\left(\boldsymbol{p}, -\frac{\boldsymbol{q}}{2} \to \boldsymbol{p}', \frac{\boldsymbol{q}}{2}\right)\hat{\rho}_p(\boldsymbol{q})\right\} - \frac{1}{4}\mathrm{Tr}_2\left\{\hat{M}_{pn}\left(\boldsymbol{p}, -\frac{\boldsymbol{q}}{2} \to \boldsymbol{p}', \frac{\boldsymbol{q}}{2}\right)\hat{\rho}_n(\boldsymbol{q})\right\}. \quad (4)$$

The relativistic density matrix $\hat{\rho}$ depends only on the momentum transfer q, as follows:

$$\hat{\rho}(\boldsymbol{q}) = \rho_S(q) + \gamma_2^0\rho_V(q) - \frac{i\boldsymbol{\alpha}_2 \cdot \boldsymbol{q}}{2m}\rho_T(q), \quad (5)$$

where each term is a Fourier transformation of a coordinate-space density;

$$\rho_S(q) = 4\pi\int_0^\infty j_0(qr)\rho_S(r)r^2dr, \quad (6)$$

$$\rho_V(q) = 4\pi\int_0^\infty j_0(qr)\rho_V(r)r^2dr, \quad (7)$$

$$\rho_T(q) = -4\pi m\int_0^\infty \frac{j_1(qr)}{q}\rho_T(r)r^2dr. \quad (8)$$

Nuclear densities, provided by the relativistic mean-field theory [12], are described in terms of upper and lower components as follows:

$$\rho_S(r) = \sum_\alpha \frac{2j+1}{4\pi}\left[G_\alpha^2(r) - F_\alpha^2(r)\right], \quad (9)$$

$$\rho_V(r) = \sum_\alpha \frac{2j+1}{4\pi}\left[G_\alpha^2(r) + F_\alpha^2(r)\right], \quad (10)$$

$$\rho_T(r) = \sum_\alpha \frac{2j+1}{4\pi}[4G_\alpha(r) \times F_\alpha(r)], \quad (11)$$

where α represents the quantum numbers of the target nucleus.

In the generalized RIA [13,14] the Feynman amplitude for NN scattering is expanded in terms of covariant projection operators $\Lambda^\rho(p)$ to separate positive ($\rho = +1$) and negative ($\rho = -1$) energy sectors of the Dirac space. The invariant amplitudes, $M_n^{\rho_1\rho_2\rho_1'\rho_2'}$, and kinetic covariants, κ_n, are given by

$$\hat{M}(p_1, p_2 \to p_1', p_2') = \sum_{\rho_1,\rho_2,\rho_1',\rho_2'} \Lambda^{\rho_1'}(p_1')\Lambda^{\rho_2'}(p_2') \times \sum_{n=1}^{13} M_n^{\rho_1\rho_2\rho_1'\rho_2'}\kappa_n\Lambda^{\rho_1}(p_1)\Lambda^{\rho_2}(p_2), \quad (12)$$

where subscripts 1 and 2 correspond to the projectile and target nucleons, respectively. The covariant projection operator $\Lambda^\rho(p)$ is defined by $\Lambda^\rho(p) = \frac{1}{2m}(\rho\ \gamma^\mu p_\mu + m)$, and kinetic covariants κ_n are constructed from the Dirac matrices. The scalar Feynman amplitude, $M_n^{\rho_1\rho_2\rho_1'\rho_2'}$, consists of the direct and exchange parts, each of which represents a sum of four Yukawa terms characterized by coupling constants, masses, and cutoff masses. In the present calculation, the IA2 parametrization of Refs. [13,14] is used.

By substituting Eq. (2) into Eq. (1) and replacing the momenta with appropriate operators, the coordinate-space Dirac equation is obtained as follows:

$$\{\gamma^0 E + i\boldsymbol{\gamma}\cdot\nabla - m - \tilde{U}(\boldsymbol{r})\}\tilde{\Psi}(\boldsymbol{r}) = 0, \quad (13)$$

where $\tilde{U}(\boldsymbol{r})$ has five potential terms as in Ref. [14] and is described as

$$\tilde{U}(\boldsymbol{r}) = \tilde{S}(r) + \gamma^0\tilde{V}(r) - i\boldsymbol{\alpha}\cdot\hat{\boldsymbol{r}}\tilde{T}(r) - \{\tilde{S}_{LS}(r) + \gamma^0\tilde{V}_{LS}(r)\}\,\boldsymbol{\sigma}\cdot\boldsymbol{L}. \quad (14)$$

The local form of the optical potential is obtained by the prescriptions given in Ref. [14], namely the asymptotic value of the momentum operator and the angular averaged expression for nucleon exchange amplitudes, which have been expected to be rather good at high energy scattering.

Equation (13) is written as two coupled equations for the upper ($\tilde{\psi}_U$) and lower ($\tilde{\psi}_L$) components, and solving for $\tilde{\psi}_U$ and using the form $\tilde{\psi}(\boldsymbol{r})_U = K(r)\phi(\boldsymbol{r})$ in order to remove the first derivative terms yields the following Schrödinger equation for $\phi(\boldsymbol{r})$:

$$\{-\nabla^2 + 2E(U_{ce} + U_{ls}\,\boldsymbol{\sigma}\cdot\boldsymbol{L})\}\phi(\boldsymbol{r}) = \{(E - V_C)^2 - m^2\}\phi(\boldsymbol{r}), \quad (15)$$

where Coulomb potential V_C is explicitly written. Although the IA2 potentials are used, it may be useful to display the form of the potentials for the simpler IA1 case. The Schrödinger equivalent potentials for IA1 parametrization are given as follows:

$$U_{ce} = \frac{1}{2E}\left\{2EV + 2mS - V^2 + S^2 - 2VV_C + \left(T^2 - \frac{T}{A}\frac{\partial A}{\partial r} + 2\frac{T}{r} + \frac{\partial T}{\partial r}\right) + \left(-\frac{1}{2r^2A}\frac{\partial}{\partial r}\left(r^2\frac{\partial A}{\partial r}\right) + \frac{3}{4A^2}\left(\frac{\partial A}{\partial r}\right)^2\right)\right\}, \quad (16)$$

$$U_{ls} = \frac{1}{2E}\left\{-\frac{1}{rA}\left(\frac{\partial A}{\partial r}\right) + 2\frac{T}{r}\right\}, \quad (17)$$

$$A = \frac{1}{E+m}t(E - V + m + S - V_C). \quad (18)$$

This IA1 parametrization corresponds to well-known five-term expansion and is obtained by setting $\rho_i = \rho_i' = +1$ ($i = 1,2$) and $n_{\max} = 5$ in Eq. (12), instead of $n_{\max} = 13$. In this case $K(r) = \sqrt{A}$ and comes to 1 as $r \to \infty$.

III. RESULTS

Table I shows root-mean-square radius of ^{4}He nucleus. On the table, "tma" in the first column corresponds to the result

TABLE I. Root-mean-square radius of proton and neutron distributions for ^{4}He.

Model	Proton	Neutron
tma	2.150	2.137
tmav1	1.452	1.443
tmav2	1.720	1.068
Charge	1.457(4)	

for relativistic mean field calculation and provides rather large radii for both protons and neutrons. Modified distributions are tmav1 and tmav2, which are obtained by compressing the profiles given by relativistic mean field calculation according to following prescription [15]:

$$Z = 4\pi \int \rho_p(r) r^2 dr = 4\pi a^{-3} \int \tilde{\rho}_p(x) x^2 dx, \quad (19)$$

$$A - Z = 4\pi \int \rho_n(r) r^2 dr = 4\pi a^{-3} \int \tilde{\rho}_n(x) x^2 dx, \quad (20)$$

where $r = x/a$ and A, Z are the nuclear mass number and the atomic number, respectively. The distributions $\rho_p(r)$ and $\rho_n(r)$ denote the proton and neutron densities given by the relativistic mean field calculation. The parameter a is such a scaling parameter that the profile $\tilde{\rho}_N(r)$ $(N = p,n)$ describes an expanded distribution for $a > 1$ and a compressed one for $a < 1$ with respect to relativistic mean field densities $\rho_N(r)$. As expected for $a = 1$, the profile $\tilde{\rho}_N(x)$ is the same as the density of the relativistic mean field. Since the contributions of tensor density are known to be small, scalar and vector densities are considered in the present calculations, and the same scale parameter is taken for both scalar and vector densities. For reference, "charge" in the table means proton nuclear radius calculated with charge radius, which is provided in terms of electron scattering [16].

Figure 1 provides proton and neutron distributions for ^{4}He with linear scale in upper panels and logarithmic scale in lower ones. Solid, dotted, and dot-dashed lines correspond to results for tma, tmav1, and tmav2, respectively. It is seen that tmav1 has compressed distributions of both protons and neutrons, in which the parameter a is chosen so as to give similar root-mean-square radius of proton to that determined by the charge radius. On the other hand, tmav2 has a more compressed neutron distribution and more expanded proton one in comparison with tmav1. This tmav2 is just a fictitious model to contrast with tmav1, which is expected to be a realistic distribution for ^{4}He. The parameters of tmav2 are chosen so as to reproduce the differential cross section at 71 MeV in the angles up to 80 deg.

In Fig. 2 observables of proton-elastic scattering from ^{4}He are shown at 71, 300, and 500 MeV, respectively. Since IA2 parameters of NN amplitude are given from 100 MeV to 1 GeV at intervals of 50 MeV [17], the proton incident energy is fixed at 71 MeV and parameters of 100 MeV are used for the calculation of 71 MeV. Results only for tmav1 (solid) and tmav2 (dot-dashed) are given. Both distributions reproduce similar profiles of differential cross section at all energies considered here, while precisely tmav2 always gives larger

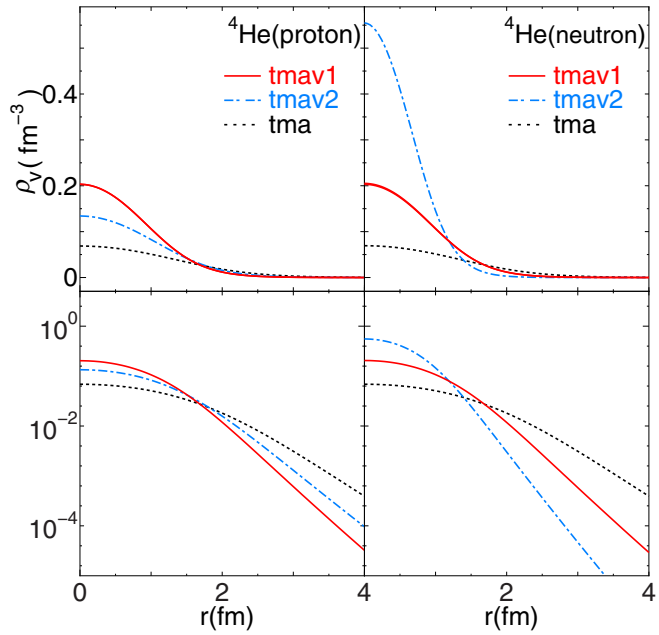

FIG. 1. (Color online) Density distributions of protons and neutrons for ^{4}He. The upper panels show the linear-scale distributions, and lower ones show the logarithmic-scale distributions. Solid, dotted, and dash-dotted lines denote the model distributions for tmav1, tmav2, and tma, respectively.

values of the cross section in the large-angle region. On the other hand, analyzing power data at 300 and 500 MeV favor the result for tmav1, although both distributions fail in reproducing A_y data at 71 MeV. In such low energies the impulse approximation may not be suitable for the calculations.

Schrödinger equivalent optical potentials for ^{4}He at 71, 300, and 500 MeV are shown in Fig. 3. Both real and imaginary parts of the central optical potential are given on the upper panels, and a characteristic structure of RIA appears in the real part of the potential, i.e., the wine-bottle shape. Since tmav2 has large neutron density in the central region, the behavior of both parts of the potentials given by tmav2 is different from those by tmav1 around the center of the nucleus, especially in the low energy. As for the spin-orbit potentials given on the lower panels, shapes of the potentials are similar for tmav1 and tmav2 in all energies while absolute values of the central region are significantly different because of the neutron distribution. Such difference of the potentials in the central region makes small contribution to the observables at angles shown in Fig. 2, especially in low energies, almost similar values of the potentials in surface region provide similar values of the differential cross section and the analyzing power. In higher energies the inner part of the potentials contributes to the observables much more, and this appears in the observables in the large-angle region at 300 and 500 MeV. Another characteristic feature of RIA is positive imaginary part of the spin-orbit potential, which is clearly seen in Fig. 3.

Table II shows root-mean-square radius of ^{6}He nucleus. In the table, tma and charge in the first column are the same in Table I. Modified distributions are tmav1, tmav2, and tmav3, which are obtained by compressing the proton and expanding

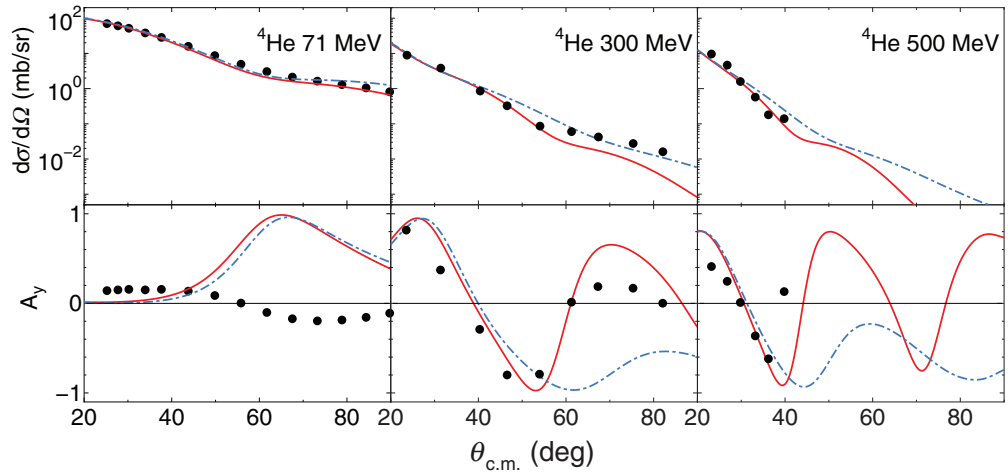

FIG. 2. (Color online) Observables of proton elastic scattering from ^{4}He at 71, 300, and 500 MeV. Each column is composed of differential cross section (upper panel) and analyzing power (lower panel). Dots are experimental data for 71 MeV [18], 300 MeV [19], and 500 MeV [20]. Solid lines are results for tmav1 and dot-dashed lines are the results for tmav2.

neutron profiles in different way. As easily seen tmav1 has the same neutron distribution as tma, i.e., the result of RMF, and has a compressed proton one with the same root-mean-square radius as that determined by the charge radius. The model of tmav2 is a fictitious one as well, as in the case of ^{4}He, but has a compressed proton distribution and an expanded neutron one. The parameters are also chosen to give good agreement with experimental data of the differential cross section at 71 MeV. The third modified distribution is composed of ^{4}He, which is compressed so as to have the same proton radius as that given by the charge radius, and a neutron density with larger radius.

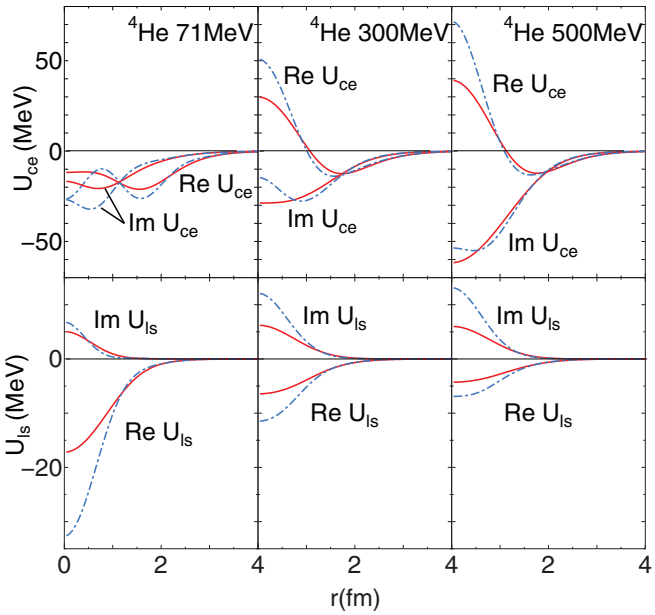

FIG. 3. (Color online) Schrödinger equvalent optical potentials for ^{4}He at 71, 300, and 500 MeV, respectively. Real and imaginary parts of the central potential are given in upper panels, and those of the spin-orbit potential are given in lower panels. The expression of lines is the same as that in Fig. 2.

Figure 4 provides proton and neutron distributions for ^{6}He with linear scale in upper panels and with logarithmic scale in lower panels. Solid, dashed, dot-dashed, and dotted lines correspond to results for tmav1, tmav2, tma3, and tma, respectively. As mentioned above tmav3 (dot-dashed line) is given by ^{4}He core + two neutrons, and large neutron density around the center of ^{6}He appears in Fig. 4 as well as the spreading neutron density in the outer region $r \geqslant 3$ fm.

In Fig. 5 observables of proton-elastic scattering from ^{6}He are shown for 71 MeV on the left side and for 0.7 GeV on the right side. All distributions give good agreement with the differential cross-sectional data at 71 MeV, while as in the case of the ^{4}He nucleus they fail to reproduce analyzing power. In the region larger than 40 deg, distributions give different values of A_y; in particular, the distribution which has large value of the nuclear density in the vicinity of nuclear center provides larger values of the analyzing power around 50 deg and smaller values in the angle region larger than 70 deg. Such large values of the analyzing power in the region between 40 and 50 deg have also appeared in the calculations of Refs. [7,8] and some cases of Ref. [10].

For 0.7 GeV, observables are shown with respect to square of transfer momentum in accordance with experimental data. All distributions slightly underestimate the differential cross section in the region larger than 0.04 (GeV/c)^2. The same underestimation also appears in Ref. [21]. Significant difference among results for different density distributions is

TABLE II. Root-mean-square radius of proton and neutron distributions for ^{6}He.

Model	Proton	Neutron
tma	2.044	3.050
tmav1	1.937	3.050
tmav2	1.635	3.352
tmav3	1.936	3.214
Charge	1.938(23)	

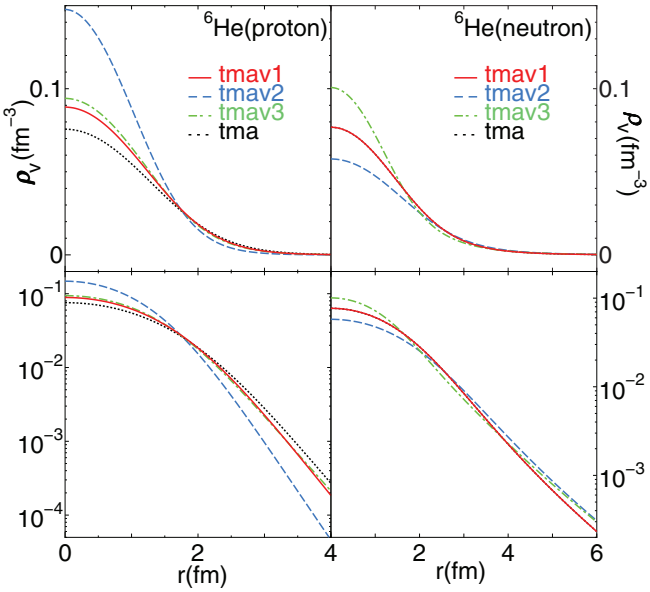

FIG. 4. (Color online) Proton and neutron distributions for ^{6}He with linear scale in upper panels and distributions with logarithmic scale in lower panels. Solid, dashed, dot-dashed, and dotted lines correspond to results for tmav1, tmav2, tma3, and tma, respectively.

seen in the region larger than 0.1 (GeV/c)^2 in both the cross section and the analyzing power. The similar relation between the central nuclear density and the analyzing power appears as well as in the case of 71 MeV.

Schrödinger equivalent optical potentials for ^{6}He at 71 and 0.7 GeV are shown in Fig. 6. Results for 71 MeV are given on the left side and for 0.7 GeV on the right side. In this case

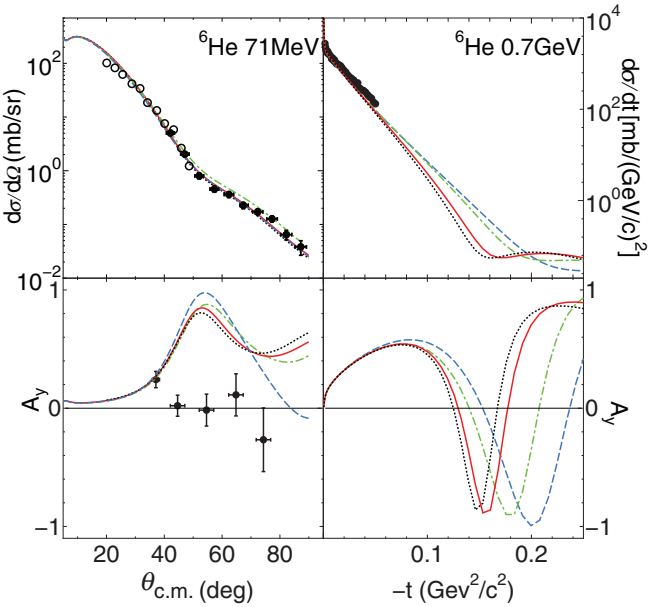

FIG. 5. (Color online) Observables of proton-elastic scattering from ^{6}He at 71 MeV and 0.7 GeV. Experimental data are taken from Refs. [1,22] for 71 MeV and Ref. [23] for 0.7 GeV. The line indication is the same in Fig. 4.

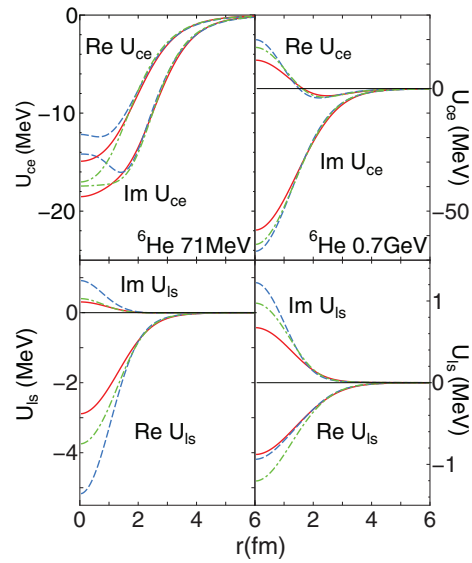

FIG. 6. (Color online) Schrödinger equvalent optical potentials for ^{6}He at 71and 0.7 GeV. Real and imaginary parts of the central potential are given in upper panels and those of the spin-orbit potential in lower panels. The expression of lines is the same as that in Fig. 4.

the scales of the potentials are different between 71 MeV and 0.7 GeV, and results for tma are omitted as well as in the case of ^{4}He. The range of the imaginary parts of the potentials is smaller than that of the real parts except the central potential at 0.7 GeV, and this is also seen in RIA calculations for many other target nuclei, known as the wine-bottle shape of the real central potential. Although the real spin-orbit potential at 71 MeV seems similar to the result shown in Ref. [9] and the imaginary part is very small, calculated analyzing powers are significantly different. As clearly seen, the depths of the central potential are smaller for both real and imaginary parts. Side-by-side comparison between the real spin-orbit potentials shows that the range and depth of the potential are slightly larger than those of Ref. [9]. Such results give rise to the similar structures of the differential cross sections and significantly different values of the analyzing power at 71 MeV.

Table III shows root-mean-square radius of ^{8}He nucleus. In the table, tma and charge in the first column are the same in Tables I and II. In order to show how much the distributions contribute to the observables, model distributions are considered as well as in the cases of ^{4}He and ^{6}He. In the models, tmav0 is the density distribution in which both proton

TABLE III. Root-mean-square radius of proton and neutron distributions for ^{8}He.

Model	Proton	Neutron
tma	1.975	3.193
tmav0	1.885	3.048
tmav1	2.634	2.873
tmav2	1.882	3.315
tmav3	1.874	3.184
Charge	1.885(48)	

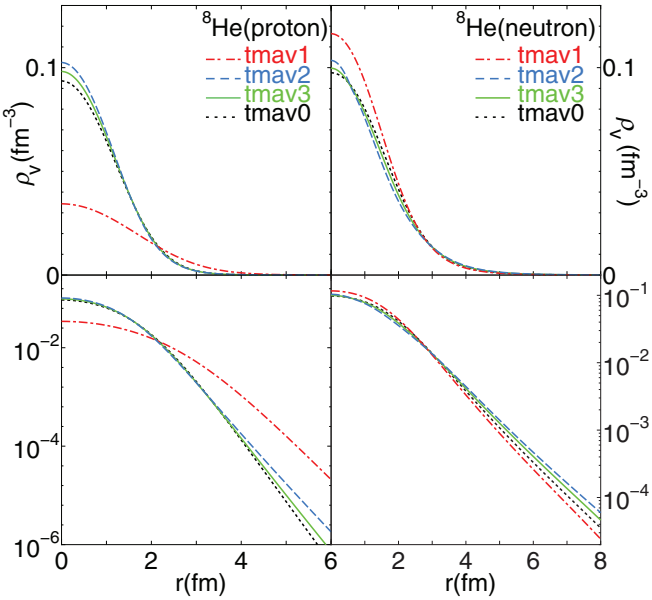

FIG. 7. (Color online) Proton and neutron distributions for ^{8}He with linear scale in upper panels and distributions with logarithmic scale in lower panels. Dot-dashed, dashed, solid, and dotted lines correspond to results for tmav1, tmav2, tma3, and tma0, respectively.

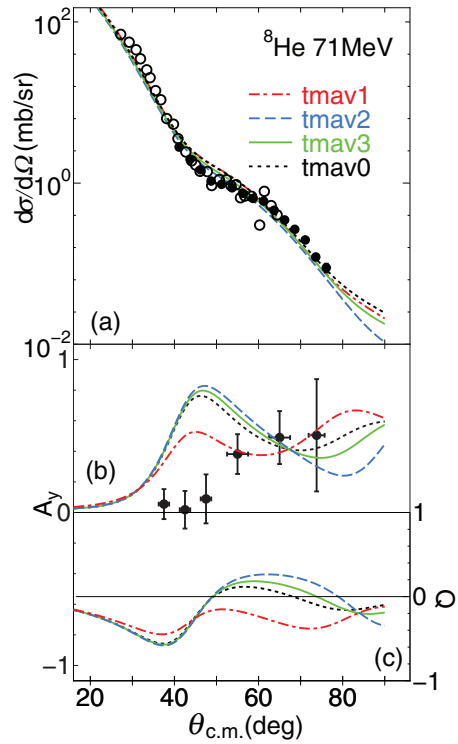

FIG. 8. (Color online) Observables of proton elastic scattering from ^{8}He at 71 MeV. Solid and open circles are experimental data taken from Refs. [3,4]. The expression of lines is the same as that in Fig. 7.

and neutron profiles are compressed with the same value of parameter "a" so that the root-mean-square radius of proton comes to the value deduced from the charge distribution. In the model tma1, the proton distribution is expanded and the neutron one is compressed with different values of the parameter. They are chosen to provide a prediction as good as possible for the data of differential cross section. This fictitious model is similar to that of ^{4}He. The models of tmav2 and tmav3 have the similar proton root-mean-square radius as that of charge distribution. The distributions of tmav2 are based on the profile for ^{4}He core + four neutrons, while tmav3 is based on the profile for ^{6}He core + two neutrons.

Figure 7 shows the density distributions according to Table III, in the same manner as Figs. 1 and 4, i.e., the left side for proton and the right side for neutron, and the upper panel is in linear scale and the lower panel is in logarithmic scale. Dot-dashed, dashed, solid, and dotted lines correspond to results for tmav1, tmav2, tma3, and tma0, respectively. Every model distribution except tmav1 shows similar profiles, although the root-mean-square radii of neutron are rather different.

Observables of proton elastic scattering from ^{8}He nucleus are shown in Fig. 8. Results given in panels (a), (b), and (c) are the differential cross section, analyzing power, and spin-rotation function, respectively. All distributions for ^{8}He provide good agreement at least with the differential cross section at 71 MeV while they fail in reproducing analyzing power data in the same as ^{4}He and ^{6}He. Such behavior of the analyzing power is also seen in Refs. [5,7]. The fictitious model tmav1, however, shows rather good agreement with A_y in the region larger than 50 deg and provides smaller values of the spin-rotation function than those of other models.

Figure 9 shows the Schrödinger equivalent optical potentials for ^{8}He nucleus at 71 MeV. Real and imaginary parts of the central potential are given in the upper panel and those of the spin-orbit potential in the lower panel. Significantly different values of the potentials are seen in radii smaller than 1.5 fm for the real part of the central potential and in radii smaller than 2.0 fm for the other ones. Such differences appear in the scattering observables in the large-angle region, which are shown in Fig. 8. As for the spin-orbit potential, tmav1 provides almost zero for the imaginary part and small absolute value for the real part accidentally. Such potential causes small values of spin observables, and in consequence calculated results with the potential seem to give good agreement with A_y data. However, this model distribution has an unrealistic value of the proton root-mean-square radius, and the actual reason for small spin-orbit potential that explains the analyzing power data should be attributed to things other than the density distribution.

As seen in the case of the ^{4}He nucleus, scattering observables, especially the analyzing powers at 300 and 500 MeV, show significant difference in the density distributions because the inner part of the nuclear distributions contributes at higher energies than 71 MeV. There are no data of spin observables for ^{6}He and ^{8}He at such higher energies and for future comparison between experimental data and calculation results scattering observables are predicted for ^{6}He and ^{8}He at 200 MeV.

Figure 10 shows observables of proton elastic scattering from ^{6}He (left side) and ^{8}He (right side), respectively, and corresponding optical potentials are given in Fig. 11. In Fig. 10, as in Fig. 8, panels (a), (b), and (c) show the differential cross section, analyzing power, and spin-rotation

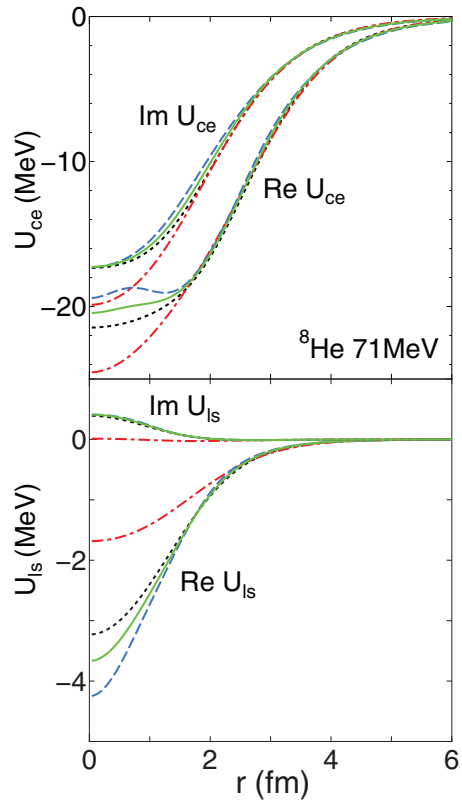

FIG. 9. (Color online) Schrödinger equvalent optical potentials for ^{8}He at 71 MeV. Real and imaginary parts of the central potential are given in the upper panel and those of the spin-orbit potential in the lower panel. The expression of lines is the same as that in Fig. 7.

function, respectively. As seen in the case of ^{4}He, a significant difference of A_y in the density distributions appears in the region larger than 50 deg for ^{6}He and larger than 30 deg for ^{8}He. Experimental data with appropriate accuracy are expected in the angle regions at 200 and 71 MeV in order to obtain information on the density distributions of helium isotopes.

Figure 11 shows Schrödinger equivalent optical potentials corresponding to Fig. 10. In the real part of the central potential the wine-bottle shape appears, except the case of tmav1 of the ^{8}He nucleus. In comparison with calculations in other higher energies, it is found that real central potential of this distribution increases with increasing proton incident energy at around nuclear center more slowly than those of other distributions. This model distribution, however, is expected to be excluded by experimental data as seen in proton-^{4}He scattering.

IV. SUMMARY AND CONCLUSION

This work has presented RIA analyses of proton elastic scattering from ^{4}He at 71, 300, and 500 MeV and from ^{6,8}He at 71 MeV, respectively. Several models of density distributions are considered, which are calculated based on RMF and with compressed and/or expanded proton and neutron density distributions.

As for the ^{4}He target, two density distributions are found, which provide good agreement with experimental data of

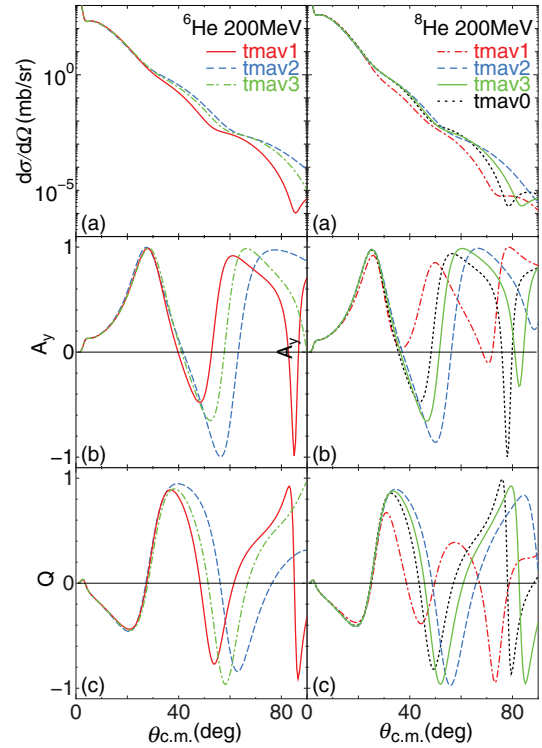

FIG. 10. (Color online) Observables of proton elastic scattering from ^{6}He and ^{8}He at 200 MeV. Results given in panels (a), (b), and (c) are the differential cross section, analyzing power, and spin-rotation function, respectively. The expression of lines for ^{6}He is the same as that in Fig. 4 and for ^{8}He in Fig. 7.

differential cross sections at all energies considered here; however, there are different profiles of analyzing power at large angles for higher energies: 300 and 500 MeV.

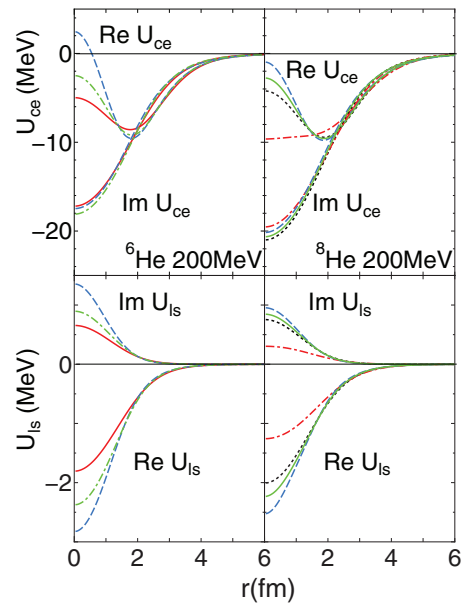

FIG. 11. (Color online) Schrödinger equivalent optical potentials for ^{6}He and ^{8}He at 200 MeV. The expression of lines for ^{6}He is the same as that in Fig. 4, and for ^{8}He in Fig. 7.

The experimental data favor the density distribution which has the same proton root-mean-square radius as that deduced from the charge radius determined by electron scattering.

The situation of differential cross section for ^{6}He nucleus is similar as ^{4}He; namely, all different density distributions provide good agreement with experimental data at 71 MeV (also at 0.7 GeV). For analyzing power, however, each distribution fails in reproducing the data at 71 MeV. The predictions of the scattering observables (the differential cross section, analyzing power, and spin-rotation function at 200 MeV) are given in the present work. The distribution which has the similar proton root-mean-square radius determined from the charge radius is expected to be favored by the experimental data at 200 MeV as well as in the case of ^{4}He.

For ^{8}He nucleus results are almost similar to other two isotopes. Model distributions provide good agreement with the data of differential cross section at 71 MeV; however, there is no distribution which provides good agreement with the data of analyzing power at this energy. Also, ^{6}He scattering observables at 200 MeV are calculated, and data of analyzing power may distinguish distributions.

The result that differential cross sections are reproduced well while analyzing powers are not at 71 MeV may show that a scattering mechanism other than the impulse approximation would contribute toward the analyzing power. Since the local form of the optical potential is obtained by the prescriptions known to be good at high energy in the RIA analysis, there would be a possibility that such treatment including the optimal factorization would affect the calculation of the analyzing power at such low energies as 71 MeV. Therefore, in order to determine the density distributions based on RIA calculations, data of both cross section and analyzing power are needed in the region of several hundred MeV.

ACKNOWLEDGMENTS

The authors acknowledge the use of the code of the relativistic mean field calculation provided from Y. Sugahara. Numerical calculations in this paper were performed using the facilities at the Information Processing Center of Shizuoka University.

[1] T. Uesaka *et al.*, Phys. Rev. C **82**, 021602(R) (2010).
[2] S. Sakaguchi *et al.*, Phys. Rev. C **84**, 024604 (2011).
[3] S. Sakaguchi *et al.*, Phys. Rev. C **87**, 021601(R) (2013).
[4] A. A. Korsheninnikov *et al.*, Phys. Lett. B **316**, 38 (1993).
[5] R. Crespo, J. A. Tostevin, and R. C. Johnson, Phys. Rev. C **51**, 3283 (1995).
[6] L. V. Chulkov, C. A. Berulani, and A. A. Korshenimikov, Nucl. Phys. A **587**, 291 (1995).
[7] S. P. Weppner, O. Garcia, and C. Elster, Phys. Rev. C **61**, 044601 (2000); S. P. Weppner and C. Elster, *ibid.* **85**, 044617 (2012).
[8] N. Keeley and R. S. Mackintosh, Phys. Rev. C **83**, 044608 (2011).
[9] K. Kaki, Y. Suzuki, and R. B. Wiringa, Phys. Rev. C **86**, 044601 (2012); **86**, 059904E (2012).
[10] S. Rafi, A. Bhagwat, W. Haider, and Y. K. Gambhir, Phys. Rev. C **86**, 034612 (2012).
[11] C. J. Horowitz and B. D. Serot, Nucl. Phys. A **368**, 503 (1981).
[12] Y. Sugahara and H. Toki, Nucl. Phys. A **579**, 557 (1994).
[13] J. A. Tjon and S. J. Wallace, Phys. Rev. C **35**, 280 (1987).
[14] J. A. Tjon and S. J. Wallace, Phys. Rev. C **36**, 1085 (1987).
[15] K. Kaki, H. Toki, and I. Tanihata, Nucl. Phys. A **724**, 99 (2003).
[16] P. Mueller *et al.*, Phys. Rev. Lett. **99**, 252501 (2007).
[17] S. J. Wallace (private communication).
[18] S. Burzynski, J. Campbell, M. Hammans, R. Henneck, W. Lorenzon, M. A. Pickar, and I. Sick, Phys. Rev. C **39**, 56 (1989).
[19] M. Yoshimura *et al.*, Phys. Rev. C **63**, 034618 (2001).
[20] S. M. Sterbenz *et al.*, Phys. Rev. C **45**, 2578 (1992).
[21] K. Varga, S. C. Pieper, Y. Suzuki, and R. B. Wiringa, Phys. Rev. C **66**, 034611 (2002).
[22] A. A. Korsheninnikov *et al.*, Nucl. Phys. A **617**, 45 (1997).
[23] S. R. Neumaier *et al.*, Nucl. Phys. A **712**, 247 (2002).